



Highly effective oxygen reduction reaction electrocatalysis: Nitrogen-doped hierarchically mesoporous carbon derived from interpenetrated nonporous metal-organic frameworks

Ai-dong Tan^a, Yi-fang Wang^a, Zhi-yong Fu^{a,b,*}, Panagiotis Tsiakaras^{c,d,**}, Zhen-xing Liang^{a,***}

^a Key Laboratory on Fuel Cell Technology of Guangdong Province, School of Chemistry and Chemical Engineering, South China University of Technology, Guangzhou 510640, PR China.

^b State Key Laboratory of Photocatalysis on Energy and Environment, Fuzhou University, Fuzhou 350002, PR China.

^c Laboratory of Alternative Energy Conversion Systems, Department of Mechanical Engineering, School of Engineering, University of Thessaly, Pedion Areos, 38334 Volos, Greece

^d Laboratory of Electrochemical Devices based on Solid Oxide Proton Electrolytes, Institute of High Temperature Electrochemistry, Yekaterinburg 620990, Russia

ARTICLE INFO

Article history:

Received 16 April 2017

Received in revised form 14 June 2017

Accepted 17 June 2017

Available online 19 June 2017

Keywords:

Ion sensitivity

Hierarchically mesoporous carbon

Interpenetrated nonporous metal-organic framework

Nitrogen-doped carbon

Oxygen reduction reaction

ABSTRACT

Nitrogen-doped carbon materials with hierarchically mesoporous structure are synthesized in the present work via the pyrolysis of an interpenetrated non-porous metal-organic framework (MOF), viz. $[\text{Zn}_2(\text{TPT})(\text{BDC})_2] \cdot \text{H}_2\text{O}$ (SCUT-11, TPT = tris(4-pyridyl)triazine, BDC = 1,4-benzenedicarboxylate), as the precursor. X-ray diffraction reveals that the synthesized metal-organic framework (MOF) is of high purity of the crystalline phase, and its structure follows our previously reported SCUT-11. This triply-interpenetrated MOF features high density of Zn cations in their interwoven packing structure, which act as effective pore-forming agent to generate mesopores in final carbon. Physicochemical characterizations reveal that the resultant carbon has high specific surface area and bimodal mesopore size distribution, which originate from the removal of metal oxide and/or metal zinc. These textural features favour both oxygen mass transfer and accessibility of catalytically active sites. Electrochemical results confirm that the resultant carbon, synthesized by pyrolysis at 900 °C, shows a superior oxygen reduction reaction (ORR) activity, which is associated with high onset and half-wave potential up to 1.0 and 0.88 V, respectively. Further investigation suggests that the as-synthesized carbon catalyst exhibits a remarkable insensitivity towards anions, like sulphate and phosphate, compared with the Pt counterpart. The above features make this carbon catalyst promising to be widely used in different fuel cell types.

© 2017 Elsevier B.V. All rights reserved.

1. Introduction

In the past few decades, metal-organic frameworks (MOFs), also known as coordination polymers (CPs), assembled by metal centres and organic linkers that extend “infinitely” in at least one

dimension, are a new class of functional materials in the field of catalysis, chemical separation, sensors, gas storage, nonlinear optics, etc. [1–8]. The advantages of MOFs derive from their defined and ordered connections, controllable structures and surface area [9]. For the structural motifs, porous and interpenetrating modes are two common structural phenomena in MOF assemblies [10]. Topical research has been focused on the porous characters of MOF complexes [8,9,11–14]. Recently, pyrolysis of porous MOFs emerges as a novel self-sacrifice template way to prepare carbon materials for the electrochemical energy applications [15–19]. The carbon materials derived from MOFs present the following advantages: i) atom-level control over composition: uniform atom distribution in heteroatom-doped carbon due to the regular crystallization of organic linkers and definite structure of MOF precursors [20]; ii) pore structure: the formation of large specific surface area and hierarchical mesopores due to tuneable morphology and the

* Corresponding author at: Key Laboratory on Fuel Cell Technology of Guangdong Province, School of Chemistry and Chemical Engineering, South China University of Technology, Guangzhou 510640, PR China.

** Corresponding author at: Laboratory of Alternative Energy Conversion Systems, Department of Mechanical Engineering, School of Engineering, University of Thessaly, Pedion Areos, 38334 Volos, Greece.

*** Corresponding author at: Key Laboratory on Fuel Cell Technology of Guangdong Province, School of Chemistry and Chemical Engineering, South China University of Technology, Guangzhou 510640, PR China.

E-mail addresses: zyfu@scut.edu.cn (Z.-y. Fu), tsiak@uth.gr (P. Tsiakaras), zliang@scut.edu.cn (Z.-x. Liang).

uniformly distributed metal/metal oxide as pore-forming agent [15]. These characters may yield some favourable effects on both the kinetics and mass transfer in building non-Pt electrocatalysts for oxygen reduction reaction (ORR) [21–23]. Many porous nitrogen-doped carbon materials have been prepared by pyrolyzing traditional porous MOFs, e.g. ZIF-8, ZIF-67, ZIF-9, MOF-5 and MIL-100-Fe, which feature high specific surface area and decent electrocatalytic activity for ORR [16,24–30]. However, in contrast with the topical research towards using porous MOFs in preparing carbon catalysts, less attention has been paid to the use of interpenetrated nonporous MOF complexes as pyrolysis precursors until now. The removal of metal/metal oxide of coordination polymer frameworks after pyrolysis and acid leaching is believed to be effective in generating the final cavities of porous carbon materials [31]. As such, the pyrolysis of interpenetrated MOFs (metal-organic frameworks) may produce efficient porous channels in the resultant structure as they have high density of metal cations in the interwoven packing structure [10,32].

In this work, a N-doped hierarchically mesoporous carbon (NHMC) catalyst ranging from 2 to 30 nm was prepared, using a nitrogen containing triply-interpenetrated MOF [Zn₂(TPT)(BDC)₂·H₂O (SCUT-11, TPT = tris(4-pyridyl)triazine, BDC = 1,4-benzenedicarboxylate) as precursor [33]. To our knowledge, this is the first report that N-doped hierarchically mesoporous carbon can be produced from an interpenetrated nonporous MOF precursor. The resulted material shows a better electrocatalytic activity than does Pt/C for the ORR with onset and half-wave potential up to 1.0 and 0.88 V, respectively. Anion-sensitivity test in three acid media (viz. HClO₄, H₂SO₄ and H₃PO₄) indicates that NHMC-900 exhibits a much higher anesthesia towards both SO₄^{2−} and PO₄^{3−} anions, than does the Pt counterpart, suggesting its applicability in different types of fuel cells [34,35].

2. Experimental

2.1. Material preparation

2.1.1. Preparation of SCUT-11

In a typical synthesis procedure, a mixture of Zn(NO₃)₂·6H₂O (150 mg, 0.50 mmol), tris(4-pyridyl)triazine (TPT, 62 mg, 0.20 mmol), 1,4-benzenedicarboxylate (BDC, 50 mg, 0.30 mmol), 4.0 mL H₂O and 6.0 mL ethylene glycol mono-ethyl ether were sealed in a 25 mL Teflon-lined stainless steel reactor and heated at 125 °C for 48 h. Yellow crystals were collected by filtration and washed with EtOH. After being dried at 60 °C in an oven, SCUT-11 crystal was obtained (81 mg, 51% yield based on TPT).

2.1.2. Preparation of N-doped hierarchically mesoporous carbon (NHMC)

The catalyst precursors were prepared as follows: 500 mg (0.63 mmol) of SCUT-11 was grinded in an agate mortar for 10 min. The obtained powder, together with dicyandiamide (DCD, 106 mg) and FeCl₃ (20 mg) with a molar ratio of 5:10:1, was dispersed into 10 mL EtOH. The dispersion was then left at room temperature under stirring for drying, and yellow mixture of powders were finally obtained.

The yellow powders were transferred into a quartz boat, which was subjected to pyrolysis at high temperatures for 1 h with a heating rate of 10 °C min^{−1} in Ar (99.999%). After cooling to room temperature, the black powders were washed with 1.0 M H₂SO₄ at 80 °C for 24 h to leach out the content of metal, metal oxide and other unstable species, followed by filtration and washing with deionized (D.I.) water. The as obtained samples are designated as NHMC-x, where x refers to the pyrolysis temperature, viz. 800, 900 and 1000 °C.

For comparison, N-doped mesoporous carbon merely derived from SCUT-11 was synthesized by the above method in the absence of FeCl₃ and DCD, which are referred to as NC-MOF in text.

2.2. Physicochemical characterization

Powder X-ray diffraction (PXRD) was carried out in the 2θ range of 5–60° using a Bruker AXS D8-Advanced diffractometer at 40 kV, 30 mA with Cu Kα radiation (λ = 1.5406 Å), a scan speed of 5° min^{−1} and a step size of 0.1° in 2θ. Raman spectrum was recorded on a LabRAM Aramis system. Scanning electron microscopy (SEM) images were taken by a Zeiss Merlin system at 5 kV. Transmission electron microscopy (TEM) images were taken by a JEOL JEM-2100 system at 200 kV. X-ray photoelectron spectroscopy (XPS) measurements were carried out with a Physical Electronics PHI 5600 multi-technique system using an Al monochromatic X-ray at a power of 350 W. Nitrogen adsorption/desorption isotherms were measured at 77 K using Micromeritics TriStar II 3020 analyzer. Before adsorption measurements, each sample was outgassed under vacuum for 8 h at 100 °C. The total surface area was analyzed with the well-established Brunauer-Emmett-Teller (BET) method, and the pore size distribution was analyzed by the Barrett-Joyner-Halenda (BJH) method (>5 nm) and the Classical Kelvin Equation (<5 nm, inset of Fig. 2&S5).

2.3. Electrochemical characterization

The electrochemical tests were performed by the aid of an electrochemical workstation Zennium (Zahner) at room temperature. Saturated calomel electrode (SCE) was used as the reference electrode, and an Au gauze was used as the counter electrode. The working electrode was a rotating ring-disk (Glassy carbon disk: 5.0 mm in diameter, platinum ring: 6.5 mm inner diameter and 7.5 mm outer diameter, RRDE). The thin-film electrode on the disk was prepared as follows. 10 mg of the catalyst was dispersed in 1.0 mL Nafion/ethanol (0.84 wt% Nafion) by sonication for 120 min. Then, 10 μL of the dispersion was transferred onto the glassy carbon disk by using a pipette, yielding the catalyst loading of 0.50 mg cm^{−2}. For comparison, we also measured the ORR electrocatalytic activity of the commercial 40 wt% Pt/C catalyst (HiSPEC4000, Johnson Matthey) with a Pt loading of 20 μg cm^{−2}.

The electrolyte, including 0.10 M KOH, 0.10 M HClO₄, 0.050 M H₂SO₄ and 1.0 M H₃PO₄, was first bubbled with Ar for 60 min. Then, CV test was conducted at 20 mV s^{−1} in the potential range between 0 and 1.23 V (vs. reversible hydrogen electrode, RHE) for 20 cycles. If unspecified, the linear sweep voltammetry (LSV) curve was obtained by scanning the disk potential from 1.23 down to 0 V at 5 mV s^{−1} in the oxygen-saturated electrolyte solution under 1600 rpm; from this curve the ORR polarization curve was extracted by subtracting the capacitive current. During the data collection, the potential of the ring was set to be 0.5 V (vs. RHE) in alkaline and 1.2 V (vs. RHE) in acid environment to determine the yield of hydrogen peroxide, respectively. Herein, all potentials were calibrated by using a home-made reversible hydrogen electrode (RHE).

The H₂O₂ yield and the electron transfer number (*n*) were calculated by the following equation:

$$n = \frac{4|i_d|}{|i_d| + i_r/N} \quad (1)$$

$$\text{H}_2\text{O}_2 (\%) = \frac{2i_r/N}{|i_d| + i_r/N} \times 100 \quad (2)$$

where *i_d* is the disk current, *i_r* is the ring current, and *N* is the ring current collection efficiency (21.85%).

3. Results and discussion

SCUT-11 metal-organic framework contains two types of Zn^{2+} centers, which construct a paddle-wheel like dimer building block and a mononuclear unit (Figs. S1–S2). The linkages of the zinc centers, the TPT (tris(4-pyridyl)triazine) ligands and the BDC (1,4-benzenedicarboxylate) ligands create a 3D framework. Triply-interpenetrated packing arrangements of these networks provide high density Zn–O coordination units. The structural mode of this precursor benefits the formation of porous nitrogen-doped carbon catalyst after pyrolysis.

The powder XRD (PXRD) patterns of the as-synthesized MOF complex and the mixture precursor are shown in Fig. S3a. It is seen that the peaks of the as-synthesized MOF agree well with the simulated pattern of SCUT-11, approving its high phase purity. Some peaks in the precursor (marked by rhombus) may correspond to either DCD (dicyandiamide) or the coordination compounds of DCD and Fe^{3+} . The data suggest that the dominant component in the precursor is SCUT-11. After pyrolyzing the precursor mixture at 900 °C, the obtained carbon NHMC-900 (see Fig. S3b) shows two broad diffraction peaks in PXRD data. The stronger peak at $2\theta = 26.5^\circ$ and the weaker one at $2\theta = 44.5^\circ$ belong to the characteristic (002) and (101) crystal planes of carbon, respectively [36–38]. No diffraction peaks are observed for the components of Fe, Zn and their oxides, indicating either negligible amount or amorphous nature of them.

The morphology of NHMC (N-doped hierarchically mesoporous carbon) was investigated by scanning electron microscopy (SEM) and transmission electron microscopy (TEM) (see Fig. 1 & S4). It is found that enriched mesopores in the range of 10–30 nm are uniformly and compactly distributed in the three catalysts. On the other hand, the mesopores in NHMC-900 and NHMC-1000 exhibit quasi-regular and dense distribution, while that of NHMC-800 shows a sparser distribution. The origin of these pores can be attributed to either the removal of gathered ZnO species or the evaporation of metal Zn [31,39]. As a higher temperature benefits the particle gathering, the pores in NHMC-900 and NHMC-1000 show a denser distribution than those in NHMC-800.

The pore features are investigated by nitrogen adsorption-desorption isotherms, as shown in Fig. 2 & S5. The isotherms are basically the same and belong to typical IV type, indicating their mesoporous nature. The total specific surface area (S_{BET}) of NHMC-800, -900 and -1000 is found to be 496.4, 541.5 and 500.6 $\text{m}^2 \text{g}^{-1}$, respectively (see Table S1). All three NHMCs exhibit bimodal mesopore size distribution. For NHMC-900, the smaller mesopore is in the range of <4 nm; in comparison, the larger one shows a broad distribution ranging from 10 to 30 nm, which is consistent to the mesopores observed by SEM and TEM micrographs. The result reveals that the nonporous MOF can also serve as a precursor to build mesoporous carbon with high specific surface area. The mesopores should solely originate from the removal of metal oxide, which is described as follows. First, during pyrolysis, the SCUT-11 frameworks are decomposed, and zinc oxide can be generated thereafter [31]. As the Zn^{2+} ions among the framework of SCUT-11 are arranged in a highly ordered microscopic structure, the resultant ZnO is uniformly distributed in the carbonized framework. In the consequent acid-leaching step, the pores are left due to the ZnO removal. Second, the bimodal distribution of the pores originates from the size of the template ZnO.

The smaller mesopores are the negative replica of the primary ZnO particles, while the larger mesopores can be ascribed to either the aggregated ZnO particles or the evaporation of metal Zn [31,39]. Metal Zn can be formed by the reduction of the metal ions with both carbon and other reducing species at high temperatures [40]. The bimodal distribution pores, namely the hierarchical mesopores, are highly desirable in the electrode by facilitating both the diffusion of active species and the kinetics of the ORR [27,41–44].

Table 1

Elemental composition (at%) of the as-synthesized carbon materials.

Sample	C	N	O	Zn	Fe	N:C
NHMC-800	83.48	6.32	10.20	0	0	0.076
NHMC-900	86.25	3.92	9.83	0	0	0.045
NHMC-1000	90.63	2.16	7.21	0	0	0.024

Table 2

Content of the carbon components (at%) of the as-synthesized carbon materials.

Sample	C–C=C	C–N	C=N/C–O	C=O	COOH
NHMC-800	75.13	9.85	7.79	4.42	2.81
NHMC-900	75.89	12.91	6.10	3.57	1.52
NHMC-1000	80.51	10.98	6.23	1.83	0.45

In Raman spectra (Fig. S6), two peaks are observed at ca. 1340 and 1580 cm^{-1} , which correspond to the characteristic D and G band in carbon, respectively [45]. The $I_{\text{D}}/I_{\text{G}}$ ratios of NHMC-800, 900 and 1000 are 1.18, 1.08 and 1.05 respectively, indicating that the graphitization degree increases with the pyrolysis temperature. It is consistent to the previous studies that the graphitization proceeds at a higher temperature [46].

The XPS survey spectra (depicted in Fig. S7) are collected to analyze the elemental composition on the surface of carbon. Table 1 shows that both the nitrogen content and the N:C ratio gradually decrease with increasing pyrolysis temperature. This result is understandable as at higher temperatures more N-containing groups are decomposed [47]. Second, no metal is detected in the three samples, indicating that most metal/metal oxides have been leached out by the strong acid. This finding agrees well with the pore-forming mechanism (*vide supra*).

It is acknowledged that the chemical state of the element is of significance to the electrochemical behaviour of carbon. As such, the curve fitting of high-resolution C1s and N1s peaks is performed. The C1s peak can be deconvoluted into five peaks, which are referred to as C–C=C (~284.8 eV), C–N (~285.8 eV), C=N/C–O (~286.3 eV), C=O (~287.2 eV) and COOH (~288.3 eV), respectively (see Fig. S8) [47–50], and the content of each component is listed in Table 2.

First, the content of C–C=C gradually increases when the pyrolysis temperature increases from 800 to 1000 °C. This result agrees with the Raman analysis, indicating a positive correlation between pyrolysis temperature and graphitization degree. Second, the content of C=O and COOH shows a dramatic decrease, suggesting these groups experience serious decomposition at higher temperatures. Third, the content of C–N first increases from 9.85% to 12.91%, which then levels off to 10.98%. Such a change can be explained by considering the adverse effect between the activation and the content of dopant nitrogen. The doping degree is enhanced when the pyrolysis temperature increases (*vide infra*), yielding more graphitic nitrogen. Consequently, the content of the nitrogen-activated carbon increases. On the other hand, the content of nitrogen decreases in the process. For example, the nitrogen content drops to 2.16% at 1000 °C, which yields a slight decrease in the content of C–N. To support the above analysis, the chemical state of N is further performed. The N1s peak is resolved into four peaks centred at ca. 398.6, 399.8, 401.3 and 402.8 eV, which respectively correspond to the pyridinic-, pyrrolic-, graphitic-, and oxide-N (see Fig. S9 and Table S2) [30,51,52]. It is seen that the content of the former two components, viz. pyridinic- and pyrrolic-N, decreases when the temperature increases. The content of graphitic-N is 20.36, 40.79, and 64.21% for the three pyrolysis temperatures, confirming that the doping degree of nitrogen is gradually enhanced in this process.

Fig. 3a depicts the CV curves collected in Ar-saturated 0.10M KOH solution. It is seen that the curves are basically the same in

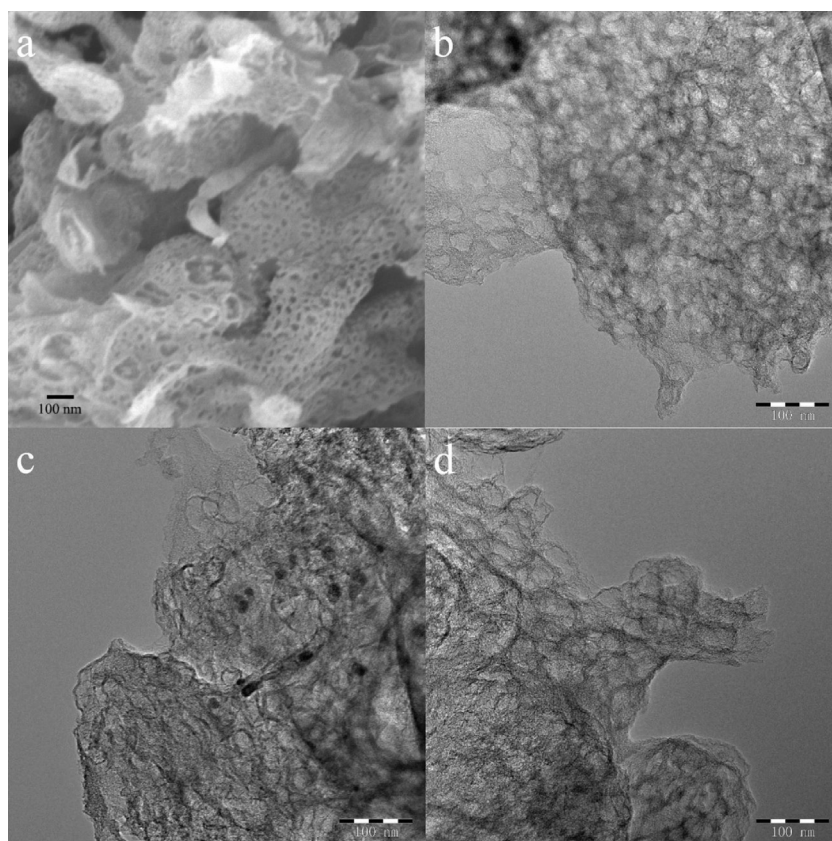


Fig. 1. (a) SEM image of NHMC-900. TEM images of: (b) NHMC-900, (c) NHMC-800, and (d) NHMC-1000.

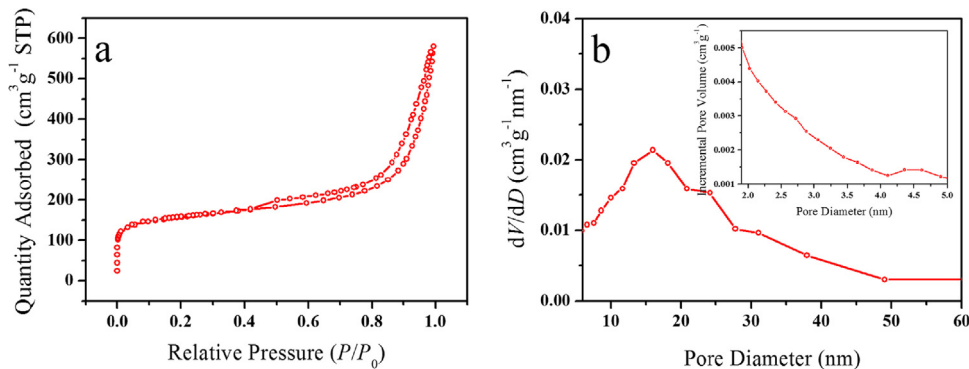


Fig. 2. (a) N_2 adsorption-desorption isotherm and (b) pore size distribution of NHMC-900.

shape with broad symmetrical peaks in the potential range 0–0.9 V, and the capacitive current decreases upon increasing the pyrolysis temperature.

First, the symmetrical peaks indicates that the electron transfer proceeds very fast, which can be attributed to the reversible sorption of hydroxyl ions onto the carbon surface. The broad shape suggests that this process occurs on a variety of functional groups with enriched electronic environments. Second, the decrease in the capacitive current is understandable as a result of the deepened decomposition of the functional groups at higher pyrolysis temperatures, which has been evidenced by XPS.

The polarization curves and the electron transfer numbers (n) in O_2 -saturated 0.10 M KOH solution are shown in Fig. 3b–c. Fig. 3b reveals that the three NHMC catalysts outperform the commercial 40 wt% Pt/C catalyst, and NHMC-900 shows the best electrocatalytic performance with an onset potential of *ca.* 1.00 V. And NHMCs are

highly selective to the 4-e transfer of oxygen, except that NHMC-1000 shows a lower electron transfer number at low potentials. To our knowledge, NHMC is one of the best N-doped carbon catalysts derived from MOFs (see Table S5).

The superior electrocatalytic activity and selectivity should originate from both the composition and structure. First, NHMC has a high specific surface area and hierarchical mesopores, which benefit fast mass transfer for oxygen and expose more active sites for catalysis. It is noted that the specific surface area follows the order of NHMC-800 < NHMC-1000 < NHMC-900, which seemingly coincides with the change in the electrocatalytic activity. Second, the monotonic decrease in the dopant nitrogen content frustrates any effect to correlate with the electrocatalytic activity, which indicates that the dopant nitrogen cannot solely act as the active sites for the ORR. In our previous work, the active sites have been claimed to be the nitrogen-activated carbon atoms [47,53].

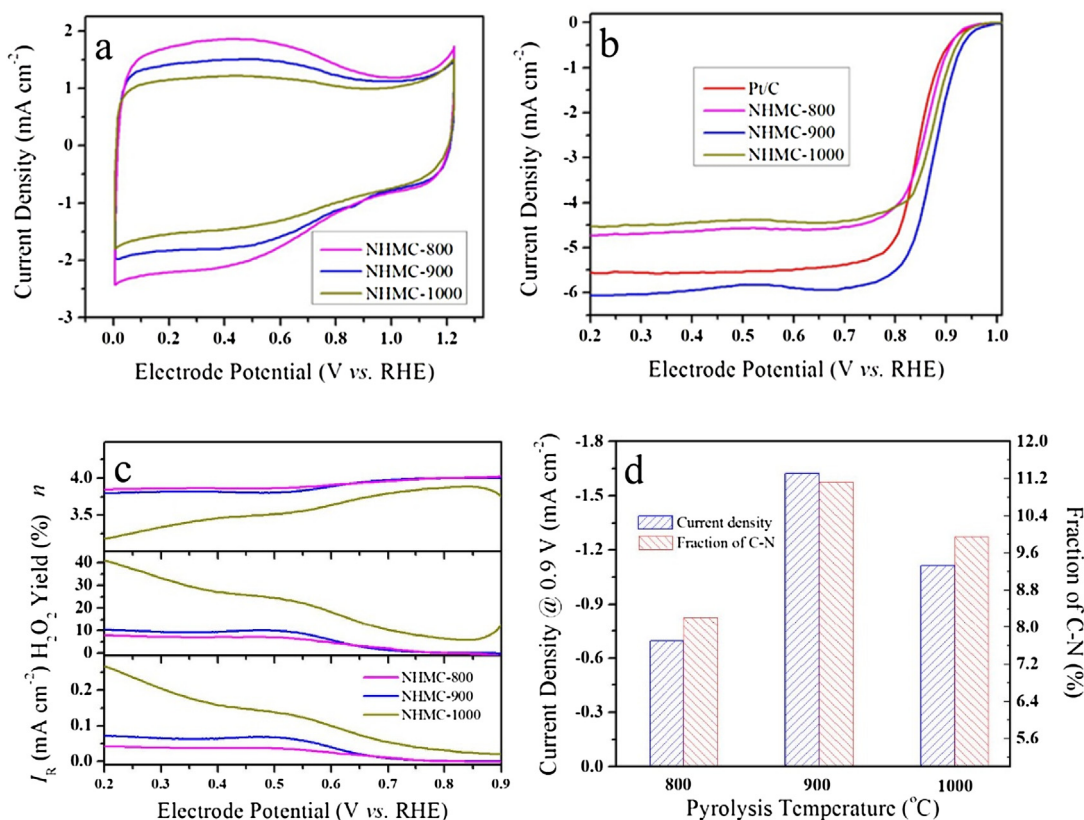


Fig. 3. (a) CV curves of the three samples at a sweep rate of 20 mV s⁻¹ in Ar saturated 0.10 M KOH. (b) ORR polarization curves of the three samples and 40 wt% Pt/C at a sweep rate of 5 mV s⁻¹ under rotating speeds of 1600 rpm in O₂-saturated 0.10 M KOH. (c) Background-corrected corresponding ring current, H₂O₂ yield and electron transfer numbers. (d) The C–N fraction derived from C1 s in XPS and the current density at 0.90 V of the above three catalysts.

The change in fraction of the nitrogen-activated carbon also follows a volcano trend with respect to the pyrolysis temperature, as discussed above. To make it clearer, the fraction of the nitrogen-activated carbon and the current density at 0.9 V are plotted in Fig. 3d vs. the pyrolysis temperature. It can be seen that both of them follow a similar trend, confirming that the nitrogen-activated carbon is indeed the active site for the ORR. Finally, it is noted that for NHMC-800 and NHMC-900 n is very close to four (3.79–3.99 in the range of 0.2–0.9 V), indicating that the ORR mainly proceeds via a 4-e transfer process. In comparison, NHMC-1000 shows a much lower n (3.18–3.88 in the range of 0.2–0.9 V), suggesting that the ORR occurs via a mixed 2- and 4-e transfer process. The XPS result reveals that NHMC-1000 is featured by graphitic-nitrogen with much less edge-type nitrogen that may be the reason for the different ORR mechanisms. The above findings indicate that the chemical configuration of nitrogen may also play a key role in determining the mechanism, although the active sites are the nitrogen-active carbon atoms.

There are disputes on the role of transition metal, e.g. Fe, in the ORR electrocatalysis. Herein, we prepared NC-MOF (Figs. S10–S12) by merely using SCUT-11 as a precursor for comparison to clarify the role of Fe (Figs. S10). It is seen that NC-MOF yields a much lower activity than does the NHMC, and the reason can be attributed to the poor intrinsic activity of the active sites in NC-MOF. This result confirms that Fe, as a catalyst, is essential in generating effective active sites during the pyrolysis, albeit it is not directly involved in catalyzing the ORR. The fraction of the nitrogen-activated carbon in NC-MOF is further quantified (see Fig. S12, Tables S2–S4), which is 8.71% in NC-MOF. The content is much lower than that of NHMC-900, which explains the difference in the electrocatalytic activity.

The intermediate-temperature fuel cells operating at 100–200 °C have a variety of advantages over the low-temperature

ones: i) fastening the kinetics, ii) improving the anti-poisoning ability against CO, NO_x and SO_x, and iii) simplifying the water management by avoiding “flooding” issue. Sulphuric acid and phosphoric acid are generally used electrolytes in intermediate-temperature fuel cells. However, the specific adsorption of the anions, viz. sulphate and phosphate, on Pt surface is acknowledged to yield a significant negative effect on the ORR [35,54–57]. Therefore, it is highly desirable to explore the anion-insensitive catalyst.

Herein, the electrocatalytic activity of NHMC is evaluated in three acid electrolytes (see Fig. 4 and Fig. S13): 0.10 M HClO₄ (pH = 1.12), 0.050 M H₂SO₄ (pH = 1.22) and 1.0 M H₃PO₄ (pH = 0.92), from which the anion-sensitivity is analyzed. First, the electrocatalytic activity of NHMC-900 remains basically the same with an onset potential of ~0.88 V vs. RHE in the three acids. In comparison, the electrocatalytic activity of Pt/C decreases in the order of HClO₄ > H₂SO₄ > H₃PO₄.

Specifically, the electrocatalytic activity of NHMC-900 is superior to that of Pt in 1.0 M H₃PO₄ (see Fig. 4c). This result indicates that the NHMC catalysts are more insensitive to the anion adsorption than Pt, which can be widely applied as Pt-alternative catalysts in different fuel cells [58].

4. Conclusions

In this work is presented a new method for the preparation of efficient nitrogen-doped carbon catalyst with hierarchically mesoporous structure by the pyrolysis of the nonporous interpenetrated MOF precursor. It is found that the high density of Zn cations in their interwoven packing structure of the interpenetrated MOF can act as an effective pore-forming agent to generate mesopores with a bimodal pore size distribution. Electrochemical results reveal that

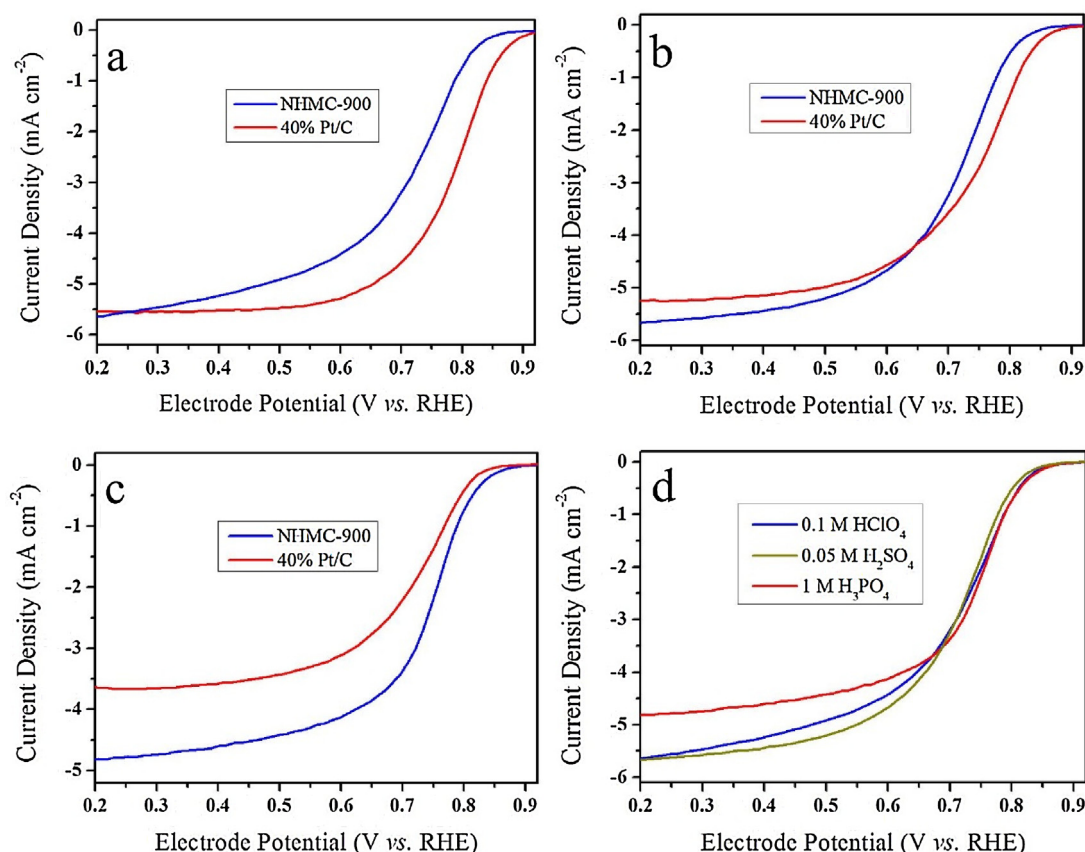


Fig. 4. ORR polarization curves of NHMC-900 and commercial Pt/C at a sweep rate of 5 mV s^{-1} under rotating speeds of 1600 rpm in O_2 -saturated (a) 0.10 M HClO_4 , (b) $0.050 \text{ M H}_2\text{SO}_4$ and (c) $1.0 \text{ M H}_3\text{PO}_4$. (d) Comparison of polarization curves in HClO_4 , H_2SO_4 and H_3PO_4 .

the textual features favour both the mass transfer of oxygen and accessibility of the active sites for catalysis. As a result, the resultant carbon shows a superior catalytic activity for the ORR and remarkable insensitivity towards the sulphate and phosphate, compared with the Pt counterpart and previously reported MOF-derived carbon catalysts. The above features make this carbon catalyst as the Pt-alternative candidate to be used in different fuel cells.

Acknowledgements

The work described in this paper was jointly supported by the National Natural Science Foundation of China (Nos. 21573076, 21476087, 21676106), Science and Technology Program of Guangzhou (201704030065), National Key R&D Program of China (No. 2016YFB0101200 (2016YFB0101204)), and the CAS Key Laboratory on Fuel Cells and Composite Electrochemical Power Sources. Prof. Tsiakaras is grateful to the “Bilateral R&D Cooperation program between Greece-China 2013–2019” and the Ministry of Education and Science of the Russian Federation (Mega-Grant, contract no. 14.Z50.31.0001) for funding.

Appendix A. Supplementary data

Supplementary data associated with this article can be found, in the online version, at <http://dx.doi.org/10.1016/j.apcatb.2017.06.051>.

References

- [1] C. Janiak, *Dalton T.* (2003) 2781–2804.
- [2] O. Toma, M. Allain, F. Meinardi, A. Forni, C. Botta, N. Mercier, *Angew. Chem. Int. Edit.* 55 (2016) 7998–8002.
- [3] A. Corma, H. Garcia, F.X.L.I. Xamena, *Chem. Rev.* 110 (2010) 4606–4655.
- [4] W.M. Bloch, N.R. Champness, C.J. Doonan, *Angew. Chem. Int. Edit.* 54 (2015) 12860–12867.
- [5] M. Eddaoudi, J. Kim, N. Rosi, D. Vodak, J. Wachter, M. O’Keeffe, O.M. Yaghi, *Science* 295 (2002) 469–472.
- [6] A. Fateeva, P.A. Chater, C.P. Ireland, A.A. Tahir, Y.Z. Khimyak, P.V. Wiper, J.R. Darwent, M.J. Rosseinsky, *Angew. Chem. Int. Edit.* 51 (2012) 7440–7444.
- [7] Y. Zeng, Z.Y. Fu, H.J. Chen, C.C. Liu, S.J. Liao, J.C. Dai, *Chem. Commun.* 48 (2012) 8114–8116.
- [8] S.M. Xie, Z.J. Zhang, Z.Y. Wang, L.M. Yuan, *J. Am. Chem. Soc.* 133 (2011) 11892–11895.
- [9] J.L.C. Rowsell, O.M. Yaghi, *Micropor. Mesopor. Mat.* 73 (2004) 3–14.
- [10] Y. Tan, H.J. Chen, J. Zhang, S.J. Liao, J.C. Dai, Z.Y. Fu, *Cryst. Eng. Comm.* 14 (2012) 5137–5139.
- [11] J.P. Zhang, X.M. Chen, *J. Am. Chem. Soc.* 131 (2009) 5516–5521.
- [12] J.L.C. Rowsell, A.R. Millward, K.S. Park, O.M. Yaghi, *J. Am. Chem. Soc.* 126 (2004) 5666–5667.
- [13] H.K. Chae, D.Y. Siberio-Perez, J. Kim, Y. Go, M. Eddaoudi, A.J. Matzger, M. O’Keeffe, O.M. Yaghi, *Nature* 427 (2004) 523–527.
- [14] B. Gole, A.K. Bar, P.S. Mukherjee, *Chem. Commun.* 47 (2011) 12137–12139.
- [15] A.J. Amali, J.K. Sun, Q. Xu, *Chem. Commun.* 50 (2014) 1519–1522.
- [16] A. Aijaz, N. Fujiwara, Q. Xu, *J. Am. Chem. Soc.* 136 (2014) 6790–6793.
- [17] L. Ge, Y. Yang, L. Wang, W. Zhou, R. De Marco, Z.G. Chen, J. Zou, Z.H. Zhu, *Carbon* 82 (2015) 417–424.
- [18] H.L. Wang, Q.L. Zhu, R.Q. Zou, Q. Xu, *Chem 2* (2017) 52–80.
- [19] L. Jiao, Y.X. Zhou, H.L. Jiang, *Chem. Sci.* 7 (2016) 1690–1695.
- [20] S.W. Liu, H.M. Zhang, Q. Zhao, X. Zhang, R.R. Liu, X. Ge, G.Z. Wang, H.J. Zhao, W.P. Cai, *Carbon* 106 (2016) 74–83.
- [21] A. Brouzgou, S.Q. Song, P. Tsiakaras, *Appl. Catal. B Environ.* 127 (2012) 371–388.
- [22] X.H. Li, K. Wan, Q.B. Liu, J.H. Piao, Y.Y. Zheng, Z.X. Liang, *Chinese J. Catal.* 37 (2016) 1562–1568.
- [23] Q.L. Zhu, W. Xia, T. Akita, R. Zou, Q. Xu, *Adv. Mater.* 28 (2016) 6391–6398.
- [24] Y.Z. Chen, C.M. Wang, Z.Y. Wu, Y.J. Xiong, Q. Xu, S.H. Yu, H.L. Jiang, *Adv. Mater.* 27 (2015) 5010–5016.
- [25] C.Y. Mao, A.G. Kong, Y. Wang, X.H. Bu, P.Y. Feng, *Nanoscale* 7 (2015) 10817–10822.

- [26] W. Zhang, Z.Y. Wu, H.L. Jiang, S.H. Yu, *J. Am. Chem. Soc.* 136 (2014) 14385–14388.
- [27] R.P. Zheng, S.J. Liao, S.Y. Hou, X.C. Qiao, G.H. Wang, L.N. Liu, T. Shu, L. Du, *J. Mater. Chem. A* 4 (2016) 7859–7868.
- [28] W. Chaikittisilp, N.L. Torad, C.L. Li, M. Imura, N. Suzuki, S. Ishihara, K. Ariga, Y. Yamauchi, *Chem. Eur. J.* 20 (2014) 4217–4221.
- [29] E. Proietti, F. Jaouen, M. Lefevre, N. Larouche, J. Tian, J. Herranz, J.P. Dodelet, *Nat. Commun.* 2 (2011).
- [30] L.J. Zhang, X.Y. Wang, R.H. Wang, M.C. Hong, *Chem. Mater.* 27 (2015) 7610–7618.
- [31] B. Liu, H. Shioyama, T. Akita, Q. Xu, *J. Am. Chem. Soc.* 130 (2008) 5390–5391.
- [32] M. Guo, Z.M. Sun, *J. Mater. Chem.* 22 (2012) 15939–15946.
- [33] Z.Y. Fu, Y. Chen, J. Zhang, S.J. Liao, *J. Mater. Chem.* 21 (2011) 7895–7897.
- [34] U.A. Paulus, T.J. Schmidt, H.A. Gasteiger, R.J. Behm, *J. Electroanal. Chem.* 495 (2001) 134–145.
- [35] P. Zelenay, B.R. Scharifker, J.M. Bockris, D. Gervasio, *J. Electrochem. Soc.* 133 (1986) 2262–2267.
- [36] D.H. Kwak, S.B. Han, Y.W. Lee, H.S. Park, I.A. Choi, K.B. Ma, M.C. Kim, S.J. Kim, D.H. Kim, J.I. Sohn, K.W. Park, *Appl. Catal. B Environ.* 203 (2017) 889–898.
- [37] P. Pachfule, D. Shinde, M. Majumder, Q. Xu, *Nat. Chem.* 8 (2016) 718–724.
- [38] J. Liu, P. Song, M.B. Ruan, W.L. Xu, *Chinese J. Catal.* 37 (2016) 1119–1126.
- [39] Z.H. Li, M.F. Shao, L. Zhou, Q.H. Yang, C. Zhang, M. Wei, D.G. Evans, X. Duan, *Nano Energy* 25 (2016) 100–109.
- [40] Y.W. Shi, X.W. Zhang, L. Wang, G.Z. Liu, *AlChE J.* 60 (2014) 2747–2751.
- [41] T.T. Sun, L.B. Xu, S.Y. Li, W.X. Chai, Y. Huang, Y.S. Yan, J.F. Chen, *Appl. Catal. B Environ.* 193 (2016) 1–8.
- [42] F.L. Meng, L. Li, Z. Wu, H.X. Zhong, J.C. Li, J.M. Yan, *Chinese J. Catal.* 35 (2014) 877–883.
- [43] J. Liang, X. Du, C. Gibson, X.W. Du, S.Z. Qiao, *Adv. Mater.* 25 (2013) 6226–6231.
- [44] M. Borghei, N. Laocharoen, E. Kibena-Poldsepp, L.S. Johansson, J. Campbell, E. Kauppinen, K. Tammeveski, O.J. Rojas, *Appl. Catal. B Environ.* 204 (2017) 394–402.
- [45] M.Y. Song, D.S. Yang, K.P. Singh, J.L. Yuan, J.S. Yu, *Appl. Catal. B Environ.* 191 (2016) 202–208.
- [46] W.H. Niu, L.G. Li, X.J. Liu, N. Wang, J. Liu, W.J. Zhou, Z.H. Tang, S.W. Chen, *J. Am. Chem. Soc.* 137 (2015) 5555–5562.
- [47] K. Wan, G.F. Long, M.Y. Liu, L. Du, Z.X. Liang, P. Tsiakaras, *Appl. Catal. B Environ.* 165 (2015) 566–571.
- [48] R. Silva, D. Voiry, M. Chhowalla, T. Asefa, *J. Am. Chem. Soc.* 135 (2013) 7823–7826.
- [49] S. Shrestha, W.E. Mustain, *J. Electrochem. Soc.* 157 (2010) B1665–B1672.
- [50] S.Y. Wang, E. Iyyamperumal, A. Roy, Y.H. Xue, D.S. Yu, L.M. Dai, *Angew. Chem. Int. Edit.* 50 (2011) 11756–11760.
- [51] G.F. Long, K. Wan, M.Y. Liu, X.H. Li, Z.X. Liang, J.H. Piao, *Chinese J. Catal.* 36 (2015) 1197–1204.
- [52] G.F. Long, X.H. Li, K. Wan, Z.X. Liang, J.H. Piao, P. Tsiakaras, *Appl. Catal. B Environ.* 203 (2017) 541–548.
- [53] K. Wan, Z.P. Yu, X.H. Li, M.Y. Liu, G. Yang, J.H. Piao, Z.X. Liang, *ACS Catal.* 5 (2015) 4325–4332.
- [54] S.Y. Lee, A. Ogawa, M. Kanno, H. Nakamoto, T. Yasuda, M. Watanabe, *J. Am. Chem. Soc.* 132 (2010) 9764–9773.
- [55] Q.F. Li, H.A. Hjuler, N.J. Bjerrum, *Electrochim. Acta* 45 (2000) 4219–4226.
- [56] Q.F. Li, J.O. Jensen, R.F. Savinell, N.J. Bjerrum, *Prog. Polym. Sci.* 34 (2009) 449–477.
- [57] Y.P. Li, L.H. Jiang, S.L. Wang, G.Q. Sun, *Chinese J. Catal.* 37 (2016) 1134–1141.
- [58] Q. Li, G. Wu, D.A. Cullen, K.L. More, N.H. Mack, H.T. Chung, P. Zelenay, *ACS Catal.* 4 (2014) 3193–3200.